



UNIVERSITY OF LEEDS

This is a repository copy of *Al₂O₃/ZnO Composite-Based Sensors for Battery Safety Applications: An Experimental and Theoretical Investigation*.

White Rose Research Online URL for this paper:

<https://eprints.whiterose.ac.uk/196911/>

Version: Accepted Version

Article:

Santos-Carballal, D orcid.org/0000-0002-3199-9588, Lupan, O, Magariu, N et al. (6 more authors) (2023) Al₂O₃/ZnO Composite-Based Sensors for Battery Safety Applications: An Experimental and Theoretical Investigation. *Nano Energy*, 109. 108301. ISSN 2211-2855

<https://doi.org/10.1016/j.nanoen.2023.108301>

© 2023, Elsevier. This manuscript version is made available under the CC-BY-NC-ND 4.0 license <http://creativecommons.org/licenses/by-nc-nd/4.0/>.

Reuse

This article is distributed under the terms of the Creative Commons Attribution-NonCommercial-NoDerivs (CC BY-NC-ND) licence. This licence only allows you to download this work and share it with others as long as you credit the authors, but you can't change the article in any way or use it commercially. More information and the full terms of the licence here: <https://creativecommons.org/licenses/>

Takedown

If you consider content in White Rose Research Online to be in breach of UK law, please notify us by emailing eprints@whiterose.ac.uk including the URL of the record and the reason for the withdrawal request.



eprints@whiterose.ac.uk
<https://eprints.whiterose.ac.uk/>

Al₂O₃/ZnO Composite-Based Sensors for Battery Safety Applications: An Experimental and Theoretical Investigation

David Santos-Carballal ^{a,*}, Oleg Lupan ^{b,c,*}, Nicolae Magariu ^c, Nicolai Ababii ^c, Helge Krüger ^b, Mani Teja Bodduluri ^d, Nora H de Leeuw ^{a,e}, Sandra Hansen ^{b,*}, Rainer Adelung ^{b,*}

^a *School of Chemistry, University of Leeds, Leeds LS2 9JT, United Kingdom*

^b *Department of Materials Science, Chair for Functional Nanomaterials, Faculty of Engineering, Kiel University, Kaiserstraße 2, D-24143 Kiel, Germany*

^c *Center for Nanotechnology and Nanosensors, Department of Microelectronics and Biomedical Engineering, Faculty CIM, Technical University of Moldova, 168 Stefan cel Mare str., MD-2004, Chisinau, Republic of Moldova*

^d *Fraunhofer Institute for Silicon Technology (ISIT), Itzehoe, Germany*

^e *Department of Earth Sciences, Utrecht University, Princetonlaan 8a, 3584 CB Utrecht, The Netherlands*

*Corresponding authors:

Rainer Adelung (ra@tf.uni-kiel.de),

Oleg Lupan (ollu@tf.uni-kiel.de, oleg.lupan@mib.utm.md),

Sandra Hansen (sn@tf.uni-kiel.de)

David Santos-Carballal (d.santos-carballal@leeds.ac.uk),

Keywords: ZnO, Al₂O₃, heterojunctions, battery safety, gas sensing

Abstract

Lithium-ion batteries are vital in one of the key nanotechnologies required for the transition to a carbon-free society. As such, they are under constant investigation to improve their performance in terms of energy and power densities. At the same time, safety monitoring is crucial, as defects in the battery cell can lead to serious safety risks such as fires and explosions as a result of the enormous heat generated in the electrolyte, causing the release of toxic and flammable gases in the so-called thermal runaway. Therefore, early and rapid detection of the gases that form before thermal runaway is of particular interest. To this end, solid-state sensors based on new heterostructured materials have gained interest owing to their high stability and versatility when used in the harsh battery environment. In this work, heterostructures based on semiconductor oxides are employed as sensors for typical components of battery electrolytes and their decomposition products. The sensors showed a significant response to vapors produced by battery solvents or degassing products, making them perfect candidates for the development of successful new prototypes for safety monitoring. Here, we have used a simple and versatile method to fabricate the Al₂O₃/ZnO heterostructure, consisting of atomic layer deposition (ALD) and thermal annealing steps. These Al₂O₃/ZnO heterostructures have shown a response to the vapours of 1,3-dioxolane (DOL, C₃H₆O₂), 1,2-dimethoxyethane (DME, C₄H₁₀O₂), LiPF₆, ethylene carbonate (EC) and dimethyl carbonate (DMC), which are typically used as components of the electrolytes in LIBs. The sensors showed a significant response to vapors produced by battery solvents or degassing products, significantly increasing the chances of developing new successful prototypes for safety monitoring. Density functional theory (DFT) calculations were employed to systematically compare the surface reactivity of the α -Al₂O₃(0001) and the ZnO(10 $\bar{1}$ 0) facets, as well as the Al₂O₃/ZnO(10 $\bar{1}$ 0) interface, towards C₃H₆O₂, C₄H₁₀O₂, nitrogen dioxide (NO₂) and phosphorous pentafluoride (PF₅), in addition to H₂O to assess the impact of relative humidity on the performance of the gas detector. The scanning tunnelling microscopy (STM) images and molecular binding energies compare well with our experiments. The energies of molecular adsorption at the heterostructure suggest that humidity will not affect the detection of the volatile organic compounds. The results presented here show that the potential to detect vapors of the components used in the

electrolytes of LIBs, combined with the size control provided by the synthesis method, makes these heterostructures extremely attractive [in devices](#) to monitor battery safety.

1. Introduction

Rechargeable lithium-ion batteries (LIBs) have impacted on sundry portable electronic devices, including cellular phones and laptops [1–4]. They also have transformed modern society by enabling and underpinning the increasingly wide use of electric vehicles. Additionally, LIBs have now started to gain a presence in the utility sector, due to their eco-friendliness and efficient storage of energy [5–7]. Their continuous development in terms of energy and power density is aimed at reducing the size and weight of the devices. In particular, the next generation of battery systems are being designed with the lowest environmental impact and highest possible theoretical energy density. For example, the widely discussed lithium-sulfur battery system, which has an energy density several times larger than current state-of-the-art lithium-ion batteries [8,9], uses elemental sulfur in the cathode and metallic lithium in the anode [4,8]. However, the use of metallic lithium presents a major challenge, as it is highly reactive and tends to form dendrites, which poses a major fire safety risk for practical applications [10]. Therefore, battery safety, which is a key aspect during the lifetime of any energy storage device, especially as energy density and thus hazard increases [9,11], cannot be determined or evaluated only by measuring changes in temperature, pressure distribution, or impedance. These properties have limitations in terms of early warning of thermal runaway in the galvanic cells of the battery. For instance, since the initial self-generated heat of the battery decreases quickly over time, the alarm level needs to be adjusted dynamically according to the practical condition of the health of the battery. On the other hand, it is difficult for the pressure sensors to monitor the occurrence of thermal runaway in a faulty battery, as the value of the electric voltage does not vanish completely [12]. Safety itself must be a priority at every step, from the selection of the materials, to the cell design, electronic controls, safety devices, and module design [9,11]. Amongst catastrophic thermal runaway risks are mechanical, electrical, and thermal abuse of LIBs, which can lead to destruction of the battery and in extreme cases also to fire [5]. Strategies to enhance the safety of LIBs include electrical protection and protection against the generation of heat and gases [5]. For example, after a cell is damaged, a stream of hot mixed gases with temperatures between 470 and 720 K can be released [13], which are a sign of thermal runaway and can finally lead to the occurrence of fire or explosion [14]. Koch et al. [13]

compared different types of sensors for the detection of changes in temperature, voltage, pressure, smoke, creep distance, force and gas during thermal runaway, concluding that the gas sensors show the fastest and strongest response of all the sensors. Thus, novel gas sensors are crucial to detect the typical decomposition products of the electrolyte from this process under harsh conditions. Solid-state materials are considered to be the most promising candidates for these sensing applications, as they operate within the same range of temperatures and provide the highest level of response. A number of investigations have been carried out in the field of monitoring and early detection of the battery thermal discharge through the use of gas sensors, resulting in different concepts of the battery management system (BMS) and different approaches to the installation of these sensors as efficiently as possible [12]. The use of gas sensors based on semiconducting metal oxides also requires resistance to temperature changes during the thermal runaway process [12]. In this context, safety devices or detectors based on semiconducting metal oxide heterostructures are highly promising, especially owing to their stability in conditions of high relative humidity or through changes of relative humidity [15], although it does require resistance to high temperatures during the thermal runaway process.

Previous studies, combining experiments with detailed computational analyses, have confirmed that semiconducting metal oxide heterostructures are appropriate for sensor applications [15,16], including battery safety systems. Moreover, these results suggest that there is an unexploited potential for developing new sensors for safety applications by exploring the gas sensing properties of layered solid-state materials, such as Al_2O_3 and ZnO and their combinations. Alumina is highly important as an ionic-covalent material, because it possesses low thermal conductivity, high melting point, and high hardness that makes it a perfect top nano-layer option for protecting sensors from dirt and corrosion in harsh battery environments, etc.

Despite several theoretical studies focusing on the bulk structure of amorphous Al_2O_3 [17–19], the surfaces of several crystalline polymorphs have been used to model the catalytic properties of this material [20–22], since they are non-polar and stable [23]. In addition, the gas detection properties of the functionalised $\text{ZnO}(10\bar{1}0)$ surface have been

evaluated by experiments complemented by density functional theory (DFT) computations [24–26].

In this study, heterostructures based on semiconductor oxides are employed as sensors for typical components of battery electrolytes and their decomposition products. The sensors showed a significant response to vapors produced by battery solvents or degassing products, significantly increasing the chances of developing successful [new](#) prototypes for safety monitoring. To understand the sensing mechanism in the synthesized sensors, *ab initio* calculations have been performed to simulate the α -Al₂O₃(0001) and ZnO (**10 $\bar{1}$ 0**) surfaces, as well as the Al₂O₃/ZnO (**10 $\bar{1}$ 0**) heterostructure, [and](#) their interaction with 1,3-dioxolane (C₃H₆O₂), 1,2-dimethoxyethane (C₄H₁₀O₂), nitrogen dioxide (NO₂), and phosphorous pentafluoride (PF₅), [in addition to](#) H₂O to evaluate the effect of humidity on the performance of the gas sensor. The binding energies and geometries of the adsorbates at the surfaces as well as charge transfers are reported and compared with our experiments. The computational results compared well with the gas sensing data.

2. Material and methods

2.1 Experimental detail

The Al₂O₃/ZnO heterostructures were grown using a synthesis from chemical solutions (SCS) technology [27,28], followed by additional atomic layer deposition (ALD) and thermal annealing steps [15], before being investigated for battery safety applications. An aqueous zinc complex solution consisting of zinc sulfate [Zn(SO₄)-7H₂O] and sodium hydroxide was used for the SCS. The ready-made solutions were diluted with deionized H₂O for the synthesis procedure. Additional information about the growth from aqueous solutions (SCS) approach has been reported previously [27,28]. The aluminum oxide layers were grown using thermal ALD (Picosun R200) at a temperature of 300 °C, while the PicoflowTM nanotechnology was employed to achieve uniform high aspect ratio (HAR) nano-layers [15]. Trimethylaluminum (TMA), which was used as the aluminum source, and water, which was employed for the oxidation of the TMA chemisorbed on the surface, were used as precursors of AlO_x and throbbed into the reaction cavity for 0.1 s per pulse to form the nanolayers. N₂ was employed to carry the precursors in vapor phase into the reactor and to remove the byproducts [15]. Thermal annealing (TA) in a furnace at 600 °C for 30 min, which was applied as a post-growth treatment, was an important procedure to enhance the crystal quality of the alumina-grown SCS films. Raman scattering experiments were carried out at room temperature with a WITec system in a backscattering configuration. The Nd: YAG laser line at 532 nm was employed with less than 10 mW power for off-resonance excitation of the specimen. The Nd: YAG laser spot was focused 10 μm below the surface of the specimen. The instrument was calibrated to the same accuracy using a silicon standard. Sensor and electrical studies were performed as described elsewhere [15]. The gas response was measured for different components of battery electrolytes and their solvents. A commonly used ether-based electrolyte, hereafter referred to as E1, was prepared as follows: 1M LiTFSI and 0.25 LiNO₃ were dissolved in a 1:1 volume ratio with 1,3-dioxolane (C₃H₆O₂) and dimethoxyethane (C₄H₁₀O₂). A commercial carbonate-based electrolyte, LP30, consisting of 1.0 M LiPF₆ in EC/DMC=50/50 (v/v), was also tested and used as received. In addition, the pure solvents 1,3-dioxolane (C₃H₆O₂) and dimethoxyethane (C₄H₁₀O₂) were also tested. All

chemicals employed, which were of analytical grade, were acquired from Merck and used without additional preparation or treatment. The concept of testing and using sensors inside the battery pack module for detection and early warning of battery thermal runaway is represented in Figure 1. The presented design assumes that the battery module is placed in a hermetic enclosure case, and the sensors covered in the protecting alumina layer are placed over the connection bars inside the case.

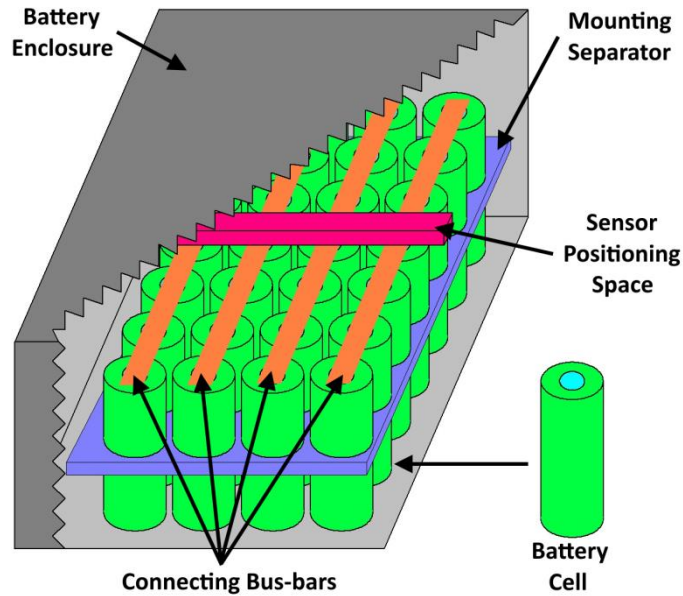


Fig. 1. Concept of sensors for the detection and early warning of battery thermal runaway.

2.2 Computational details

We have employed the Vienna Ab Initio Simulation Package (VASP) [29–32] to carry out unrestricted DFT calculations of the $\text{Al}_2\text{O}_3/\text{ZnO}$ ($10\bar{1}0$) heterojunction and the surfaces of its parent materials $\alpha\text{-Al}_2\text{O}_3(0001)$ and $\text{ZnO}(10\bar{1}0)$. Next, we investigated the interactions of the surfaces and interface with $\text{C}_3\text{H}_6\text{O}_2$, $\text{C}_4\text{H}_{10}\text{O}_2$, NO_2 , and PF_5 , as well as H_2O to elucidate the effect of moisture on the operation of the gas sensor. The Perdew, Burke and Ernzerhof (PBE) [33,34] functional, which is a gradient-corrected or semilocal approximation of the exchange-correlation energy, was employed to simulate all structures and energies. Van der Waals forces were added using the semiempirical method proposed by Grimme, with the damping of Becke-Johnson [D3-(BJ)] [35,36], which is important for a correct simulation of the molecular adsorptions [25,37–41]. The

core electrons, which were defined up to and including the $3p$ states of Zn, $2p$ of Al and P and $1s$ of O, C, N and F, were treated as frozen levels, but the $1s$ state of the H atom was considered as valence. The interaction between the core and the valence electrons was estimated employing the projected augmented wave method (PAW) [42,43]. The Kohn–Sham one-electron valence orbitals were obtained using a periodic and delocalized plane-wave basis set with a maximum allowed kinetic energy of 400 eV. The electron density was optimized self-consistently until the energy reached 10^{-5} eV. A fast inertial relaxation engine (FIRE) method [44,45], which is based on a variable time step method and does not directly depend on the curvature, was used for the geometry optimizations. The structural minimizations were considered converged when the Hellmann-Feynman forces on all atoms became smaller than $0.01 \text{ eV}\cdot\text{\AA}^{-1}$. The description of the d states of Zn was enhanced using the Dudarev approach [46] to the so-called DFT + U method [47], where we have chosen a $U_{\text{eff}} = 6.0 \text{ eV}$ [16,24–26]. These settings allowed the computation of total electronic energies differing by less than $1 \text{ meV}\cdot\text{atom}^{-1}$.

Γ -centered Monkhorst–Pack (MP) grids [48] of $5 \times 3 \times 1$ k -points were employed for the simulations in the reciprocal space of the $\text{Al}_2\text{O}_3/\text{ZnO}$ ($10\bar{1}0$) interface and the $\text{ZnO}(10\bar{1}0)$ support [49], whereas the Al_2O_3 (0001) surface was simulated using the Γ -centered MP [48] $5 \times 5 \times 1$ mesh [21]. The calculations of the isolated adsorbate species were performed considering only the Γ point of the Brillouin zone (BZ), employing a cell of broken symmetry large enough to avoid spurious interactions. To enhance the efficiency of the computations in the reciprocal space, we applied the Gaussian smearing [50,51], with a width value of 0.1 eV, to obtain the electronic partial occupancies. Furthermore, the tetrahedron method with Blöchl corrections [52–56] was employed in final single point calculations to obtain accurate electronic properties and energies.

3. Results and Discussion

3.1 Morphology and composition analyses

The surface morphology and composition of the synthesized heterostructures are analyzed in this section. Figure 2 and Figure S1 show the SEM images of the surface structure and morphology of the $\text{Al}_2\text{O}_3/\text{ZnO}$ heterostructure, indicating a dense film of

interpenetrating columnar grains. Increasing the deposition time of the ALD led to an increased thickness of the formed Al_2O_3 layer, which can be observed as a surface structuring on top of the formed columnar grains (Figure 2a-c and Figure S1a-c). It is worth noting, that for a thickness of the Al_2O_3 layer of 7 nm, almost no polycrystals appear on the surface (see Figure 2a and Figure S1), while with increasing thickness of this overlayer the polycrystallites become more pronounced (cf. Figure 2b,c and Figure S1b,c).

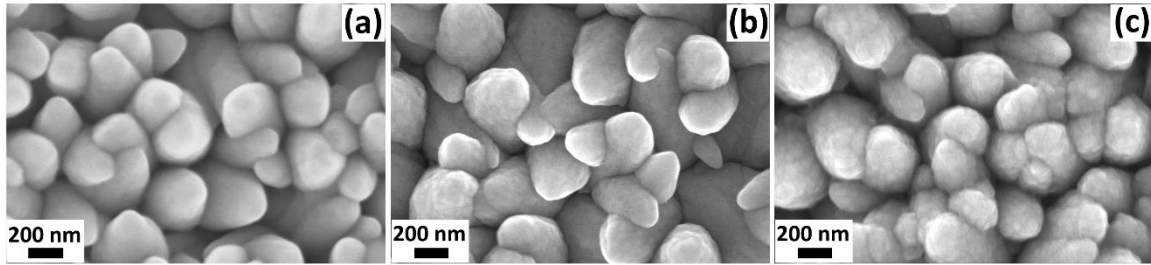


Fig. 2. Scanning electron microscopy (SEM) images of the $\text{Al}_2\text{O}_3/\text{ZnO}$ heterostructured layers after thermal annealing at 600 °C for 30 min containing a nano-layer of Al_2O_3 with a thickness of: (a) 7 nm; (b) 10 nm; and (c) 12 nm.

3.2 X-ray diffraction and Micro-Raman characterization

To study the crystallinity of the formed $\text{Al}_2\text{O}_3/\text{ZnO}$ heterostructured layers, XRD characterization was carried out. Figure 3a shows the XRD pattern of the $\text{Al}_2\text{O}_3/\text{ZnO}$ heterojunctions with a thickness of 10 nm for the Al_2O_3 layer, whereas the XRD of the $\text{Al}_2\text{O}_3/\text{ZnO}$ heterojunctions with thicknesses of 7 and 12 nm of the Al_2O_3 layer are shown in Figure S2. Regardless of the thickness of the Al_2O_3 layer, the diffraction peaks detected for all $\text{Al}_2\text{O}_3/\text{ZnO}$ heterojunctions are indicative of the ZnO ($10\bar{1}0$), (0002), ($10\bar{1}1$), ($10\bar{1}2$), ($11\bar{2}0$), ($10\bar{1}3$), ($11\bar{2}2$), ($20\bar{2}1$), and (0004) planes. The most prominent peaks were obtained for the ($10\bar{1}0$), (0002), ($10\bar{1}1$) and ($10\bar{1}3$) planes at values for 2θ of 31.77, 34.46, 36.26 and 62.85°, respectively, with the (0002) being the preferential peak. Peaks assigned to Al_2O_3 phases were not identified, which is explained by the fact that the aluminum oxide layer can be considered as amorphous or very finely particulate after thermal annealing at 600 °C [57].

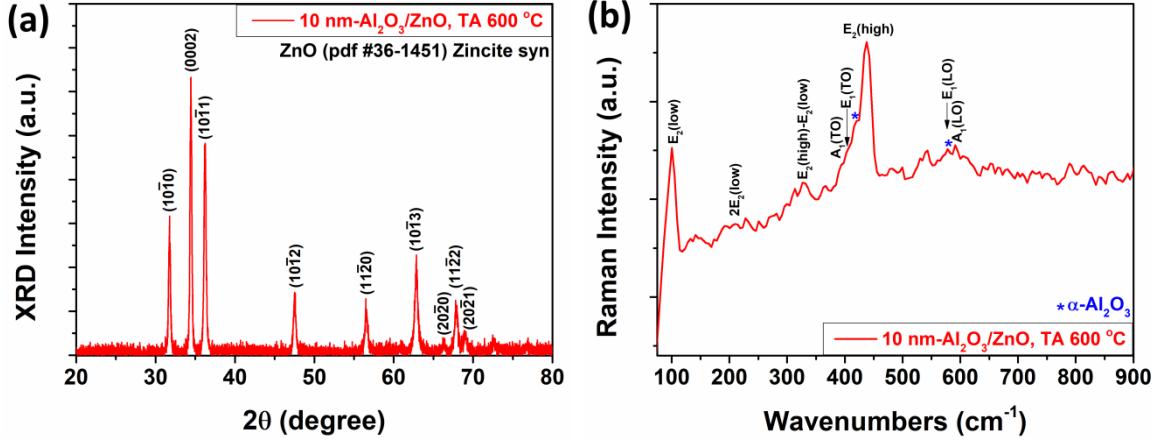


Fig. 3. (a) X-ray diffraction (XRD) pattern; and (b) micro-Raman spectrum of the 10 nm-Al₂O₃/ZnO heterostructured layers thermally annealed (TA)- treated at 600 °C for 30 min.

Micro-Raman studies provide detailed information about the quality and phase of the crystalline material, which is very important to understand the transport performance and phonon interaction with the free carriers. Micro-Raman spectra of the ALD/SCS-grown Al₂O₃/ZnO nano- and micro-structures, which were collected using the Nd: YAG laser line at 532 nm, are presented in Figure 3b within the range between 70-900 cm⁻¹. The micro-Raman spectrum of the Al₂O₃/ZnO heterostructured layers with a thickness of 10 nm for the Al₂O₃ layer after thermal annealing/treatment at 600 °C for 30 min is shown in Figure 3b. It can be seen that the highest intensity peaks are at the wavenumbers of 100 and 437 cm⁻¹, which can be assigned to the nonpolar E₂(low) and E₂(high) modes of ZnO, respectively [58,59]. It is known that ZnO with a wurtzite structure belongs to the space group C_{6v}⁴ (P6₃mc). ZnO has 12 phonon modes, and at the Γ point of the Brillouin zone, the group theory predicts the existence of the following modes: $\Gamma = A_1 + 2B_1 + E_1 + 2E_2$ [58]. The peak at about 204 cm⁻¹ is attributed to the 2E₂(low) second-order mode [60], with the one at 330 cm⁻¹ attributed to the E₂(high)-E₂(low) multi-phonon scattering [61], whereas the peaks at 385 and 410 cm⁻¹ are attributed to the A₁ (TO) and E₁ (TO) transverse optical modes, respectively. The other two peaks at 578 and 590 cm⁻¹ are ascribed to the A₁(LO) and E₁(LO) superposition modes of ZnO, respectively [59,61,62]. α -Al₂O₃ belongs to space group D_{3d} and has two formula units per primitive unit cell, which leads to the optical modes $\Gamma = 2A_{1g} + 2A_{1u} + 3A_{2g} + 2A_{2u} + 5E_g + 4E_u$ at point Γ

of the Brillouin zone. Thus, the Raman active peaks at 418 and 578 cm^{-1} are assigned to the A_{1g} and E_u optical modes, respectively, of $\alpha\text{-Al}_2\text{O}_3$ phase [63].

3.3 Gas sensing properties

Owing to the fact that resistive gas sensors present superior properties for environment detection and early warning of battery thermal runaway compared to catalytic combustion sensors, thermal conductive sensors, QCM sensors (quartz crystal and its surface selective coating), electrochemical sensors or infrared sensors [12], we decided to investigate gas detection performances of the synthesized heterojunctions with different thicknesses as resistive sensors in the presence of various components of the battery electrolytes [5,14]. At the same time, these heterostructures can also be used as a temperature sensor, as they can determine the temperature based on the electric resistance of the heterostructure. Thus, our 2-in-1 sensor operates as a temperature sensor at low temperatures and as a gas sensor at relatively high temperatures.

Figure 4 shows the schematic structure of the investigated sensor based on $\text{Al}_2\text{O}_3/\text{ZnO}$ heterostructures on a glass substrate and Au/Cr contacts in the form of a meander (Top view) and of the heater placed on the opposite side (Bottom view) to obtain the required operating temperatures.

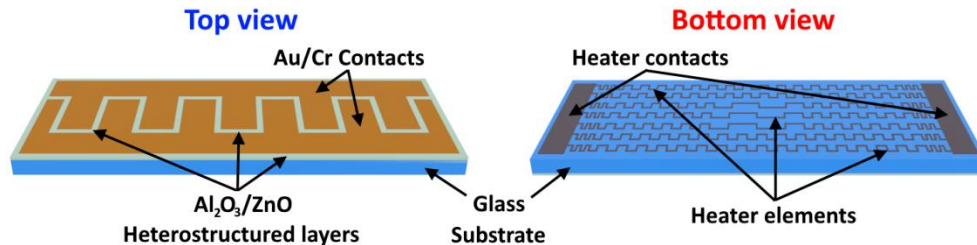


Fig. 4. Top and bottom view of the investigated sensor structure based on $\text{Al}_2\text{O}_3/\text{ZnO}$.

In order to use these heterostructures as a temperature sensor, the change in electrical resistance was studied as a function of the operating temperature (see Figure S3). Figure S3 displays the ideal characteristic (red line) of the electric resistance for semiconductors and the experimental results of the heterostructure (black line) as a function of the

temperature. From the figure, the relationship was determined using the electrical resistance at the required temperature and the following equation:

$$R = \alpha \exp\left(-\frac{T}{T_0}\right) + R_0 \quad (1)$$

where R is the calculated resistance, α is the temperature coefficient, T is the operating temperature, T_0 is the initial temperature and R_0 is the initial resistance.

Figure 5a shows the gas response of the Al₂O₃/ZnO sample to C₃H₆O₂, C₄H₁₀O₂, E1 and LP30 (100 ppm) for different thicknesses of 5, 7, 10, 12, 15 nm of the Al₂O₃ films at an operating temperature of 350 °C. The selectivity for C₃H₆O₂ is achieved for all thicknesses of the Al₂O₃ layer, with the sample containing the 10 nm layer generally showing the highest response of ~25.19%. The current-voltage characteristics at different thicknesses of the Al₂O₃ overlayer demonstrate non-linear behaviour (see Figure S4a).

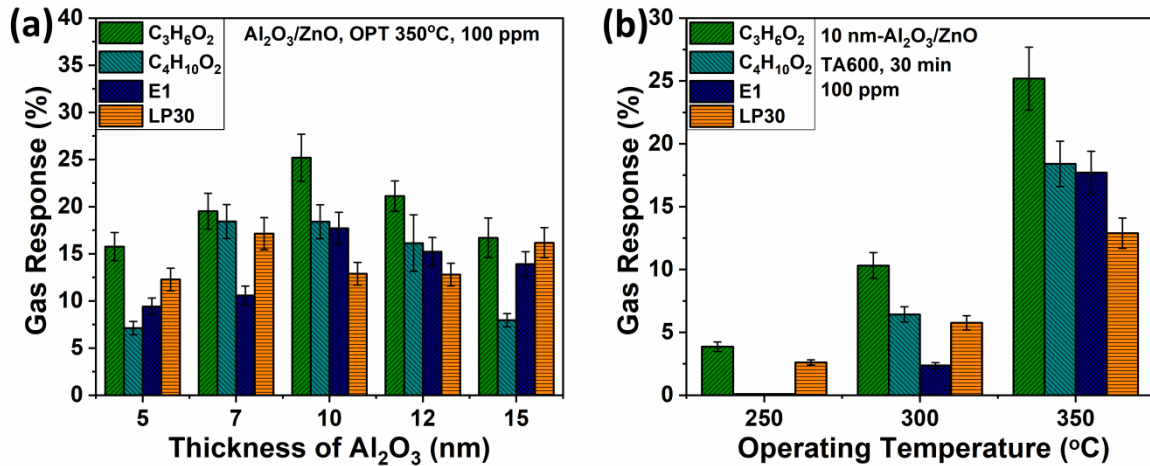


Fig. 5. (a) Gas response versus different thickness of 5, 7, 10, 12, 15 nm of the Al₂O₃ overlayer. (b) Gas response versus operating temperatures of the Al₂O₃/ZnO sample set containing the 10 nm overlayer of Al₂O₃ after thermally annealing (TA) at 600 °C for 30 min.

Figure 5b indicates that the operating temperature has a strong impact on the gas response, which increases with temperature for 100 ppm of C₃H₆O₂, C₄H₁₀O₂, E1 and LP30. At an operating temperature of 250 °C, there is only response for C₃H₆O₂ and LP30 vapors with values of ~ 4% and ~ 2.5%, respectively. However, by raising the operating temperature to 300 °C, a response occurs for all vapors with evident selectivity for C₃H₆O₂ with a

value of ~10.31%, and for $C_4H_{10}O_2$ with a value of ~6.43%. By elevating the operating temperature by 50 °C, up to the value of 350 °C, we found that the response to all vapors increases further, while the selectivity remains the same for the $C_3H_6O_2$ vapor. The current-voltage characteristics also demonstrate double non-linear characteristics, depending on the operating temperatures, see Figure S4b.

The selectivity and response to $C_3H_6O_2$ vapor was characterized at a concentration of 100 ppm, which showed the highest response for the Al_2O_3/ZnO heterostructured layers with a thickness of 10 nm for the Al_2O_3 overlayer. Subsequently, gas response measurements were performed at different concentrations of $C_3H_6O_2$ vapor (1, 5, 10, 100, 500 and 1000 ppm), which are reported in Figure 6a. The highest response of ~58% was detected at a vapor concentration of 5 ppm of $C_3H_6O_2$. Increasing the concentration of the $C_3H_6O_2$ vapor decreases the gas response, with a value of only ~24% at the highest concentration of 1000 ppm. This means that the high vapor concentration (i.e. 1000 ppm) accelerates the chemical reactions that take place during the sensing mechanism, thereby saturating the samples more quickly, see Figure S5.

Figure 6b illustrates the dynamic response to $C_3H_6O_2$ vapor of different concentrations from which the times of response and times of recovery were calculated. The response times τ_r are 21.74, 21.91 and 10.29 s, and the recovery times τ_d are >50.20, >50, and 23.83 s for the vapor concentrations of 5, 10 and 100 ppm, respectively. Figure 6b also shows that at the concentrations of 5 and 10 ppm, there is a partial recovery, but at the concentration of 100 ppm there is a total recovery after the supply of the target vapors has been stopped. Figure 6c shows the variation of the response to 5 ppm of $C_3H_6O_2$ vapor over time for the sample containing the 10 nm overlayer of Al_2O_3 , where we can observe that the response remains essentially constant.

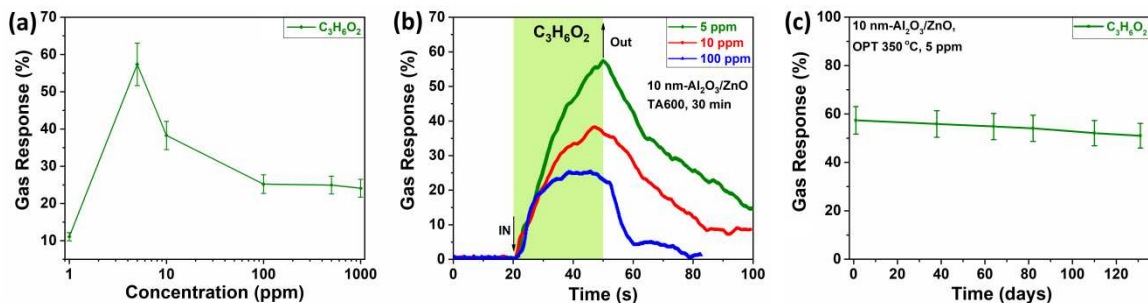


Fig. 6. (a) Response to different concentrations of $C_3H_6O_2$ of the Al_2O_3/ZnO samples set with a thickness of 10 nm of the Al_2O_3 overlayer thermally annealed (TA) at 600 °C for 30 min. (b) Dynamic response to concentrations of 5, 10 and 100 ppm of the Al_2O_3/ZnO sample set with a thickness of 10 nm of the Al_2O_3 overlayer thermally annealed (TA) at 600 °C for 30 min. (c) Variation of the gas response to 5 ppm of $C_3H_6O_2$ vapors over time for the sample containing the 10 nm overlayer of Al_2O_3 .

3.4 Sensing mechanism

Heterojunctions based on metal oxides can lead to new properties, such as improved sensitivity and selectivity, as reported in previous studies [64,65]. The use of the ALD method allowed the possibility to obtain different types of heterostructures, namely p-n, n-n, and n-p [66]. As a result, different sensors can be obtained that can detect different types of gases, from hydrogen to volatile organic compounds (2-propanol, n-butanol, acetone) [66–68]. Different oxides can be deposited by the ALD method, e.g. NiO [68], Al_2O_3 [15,69,70], TiO_2 [71] and many other types of materials. Aluminum oxide (Al_2O_3) has different α , γ , η , δ , θ and χ phases which due to their properties have different band gap lengths [72]. It is also known that the amorphous Al_2O_3 coating can increase the number of catalytic reactions that can take place at the surface of the sensor. A more detailed description of the given process is presented in the work of Zou et al. [73]. One of the main reasons for the improved sensitivity or selectivity is the interface or junction between two semiconducting metal oxides, which plays an important part in gas detection, owing to the adsorption of atmospheric oxygen at the surface of the heterojunction. In the case of zinc oxide (ZnO) structures, it leads to electron transfer from the oxide surfaces to form a specific oxygen species (O_2^- , O^- , O^{2-}) at the surface [65,74], according to the equation:



In the case of aluminum oxide (Al_2O_3), dissociation [75,76] can occur according to the equation:



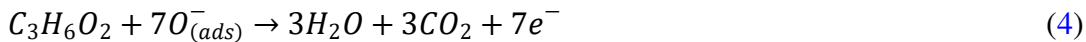
It has been suggested that different heterostructures based on Al₂O₃ can be used as insulators, owing to their *p*-type behavior [77], which can increase the number of catalytic reactions [77–79] and serve as absorption centers [80–82].

A Schottky contact was formed at the Al₂O₃/ZnO interface, due to electron transfer facilitated by the different lengths of the energy bands of aluminum oxide and zinc oxide [77]. We observed that the current-voltage characteristics are typical of the Schottky contact, which bends upward the ZnO energy band, most prominently in the case of the Al₂O₃/ZnO heterostructure with the aluminum oxide layer thickness of 10 nm.

1,3-Dioxolane, C₃H₆O₂, which is an electrolyte component commonly used in Li-S batteries [83], is a cyclic molecule of five members whose positions number 1 and 3 are occupied by oxygen atoms [84]. Cutler et al. [85] have suggested that high concentrations of the 1,3-dioxolane vapor lead to the formation of larger amounts of CO at temperatures over 1000 K. However, at low operating temperatures and low concentrations, 1,3-dioxolane decomposes into water and CO₂ [85].

Thus, upon exposure to 1,3-dioxolane gas of the Al₂O₃/ZnO heterojunction, a low-conductivity depletion region is formed at the surface, due to the presence of various oxygen species on the surface, and as a result the junction channels are narrowed and a change in the Fermi level of the Al₂O₃/ZnO heterostructure occurs. Thus, 1,3-dioxolane molecules can interact with surface oxygen ions according to Figure S6. From figure S6 it can be seen that initially the 1,3-Dioxolane molecule interacts with the adsorbed oxygen from the surface (step 1). Following the interaction of the 1,3-Dioxolane molecule with 7 adsorbed oxygens, 3 molecules of CO₂ and H₂O and 7 electrons are obtained (step 2).

The process represented in Figure S6 can be described using the following chemical reaction [5,85]:



Reaction (3) shows that a rise in the number of electrons leads to an increase in the electric current flowing through the heterojunction, explaining the large sensitivity obtained for C₃H₆O₂ vapor.

The high selectivity towards 1,3-dioxolane of the Al₂O₃/ZnO heterostructure with a 10 nm thick aluminum oxide layer can also be explained by the Debye length effect for ZnO [86–88], which can be calculated:

$$\lambda_D = \sqrt{\frac{\varepsilon kT}{q^2 n_c}} \quad (5)$$

where ε , k , T , q , and n_c are the static dielectric constant, Boltzmann constant, absolute temperature, electric charge, and charge carrier concentration, respectively.

The Debye length for n -type semiconductors can be controlled by the concentration of donors within the lattice. The Al³⁺ ions, obtained in equation (3) allow the control of the Debye length for ZnO. [89]. We found that 10 nm of thickness of aluminum oxide (Al₂O₃) is equal to the Debye length, leading to an electron-depleted region with a strong change in resistance when the gas mixture is applied, resulting in a high response. For thicknesses of aluminum oxide larger than 10 nm, the Debye length changes, which reduces the region depleted of electrons and the electrical resistance and the response to the gases.

The high selectivity of the Al₂O₃/ZnO heterostructure for 1,3-dioxolanes can be rationalized as follows:

- 1) A Schottky contact was obtained, and the most pronounced characteristic was found for 10 nm of thickness of the aluminum oxide layer. The application of the gas moves the Fermi level closer to the conduction band.
- 2) The Debye length only becomes equal to the thickness of Al₂O₃, when the latter has 10 nm, which allows the formation of a large electron depletion region, resulting in a high selectivity towards 1,3-dioxolanes.

3.5 Surfaces

Our starting point for the simulations of the surface reactions is the pristine α -Al₂O₃(0001) surface with hexagonal symmetry, the ZnO (10 $\bar{1}$ 0) facet and the Al₂O₃/ZnO (10 $\bar{1}$ 0) interface with orthorhombic symmetry. The stable non-polar,

symmetric and stoichiometric slabs [23] used to represent the α -Al₂O₃ (0001) and ZnO (10 $\bar{1}$ 0) facets were created from the bulk phase with optimised lattice parameters and internal coordinates, using the minimum energy techniques applied to dislocation, interface and surface energies' (METADISE) code [90]. We introduced a void region of 20 Å between the surface slabs, to ensure negligible interactions with neighbouring cells. The ions in the bottom layers of the simulation cell, comprising two stacking sequences, were kept frozen at their optimised positions in the bulk to mimic the extended material, whereas the ions in the remaining layers were permitted to move unconstrainedly. We included dipole corrections in the direction orthogonal to the surface [91,92], which is required to quench any dipole generated by the adsorbed molecular species [16,21,37,40,93–98], even though the actual surface slabs are non-dipolar.

The α -Al₂O₃ (0001) facet was simulated employing a cell with a large surface area of 78.16 Å², whereas the ZnO (10 $\bar{1}$ 0) facet and the Al₂O₃/ZnO (10 $\bar{1}$ 0) heterojunction were represented by simulation cells with an area of 68.22 Å². The computational slab of the α -Al₂O₃ (0001) surface consists of 100 atoms distributed in five stacking sequences comprising 4 formula units (f.u.) each. The simulation slabs of the ZnO(10 $\bar{1}$ 0) facet and the Al₂O₃/ZnO (10 $\bar{1}$ 0) interface contain 96 and 95 atoms respectively, occupying 6 double stacking sequences of 8 f.u. each. The constructed surface slabs were characterised by a minimum thickness of 9.9 Å for the α -Al₂O₃ (0001) facet and a maximum width of 14.8 Å for the ZnO(10 $\bar{1}$ 0) and Al₂O₃/ZnO (10 $\bar{1}$ 0) systems. We have rigorously tested the number of relaxed and total layers as well as the size of the vacuum gap until we achieved an energy convergence below 1 meV per atom.

The stacking of the ionic planes is (Al)–(O₃)–(Al) for the most stable termination of the α -Al₂O₃ (0001) surface [21], with the ions within parentheses located roughly in the same layer, as illustrated in Figure 7a.

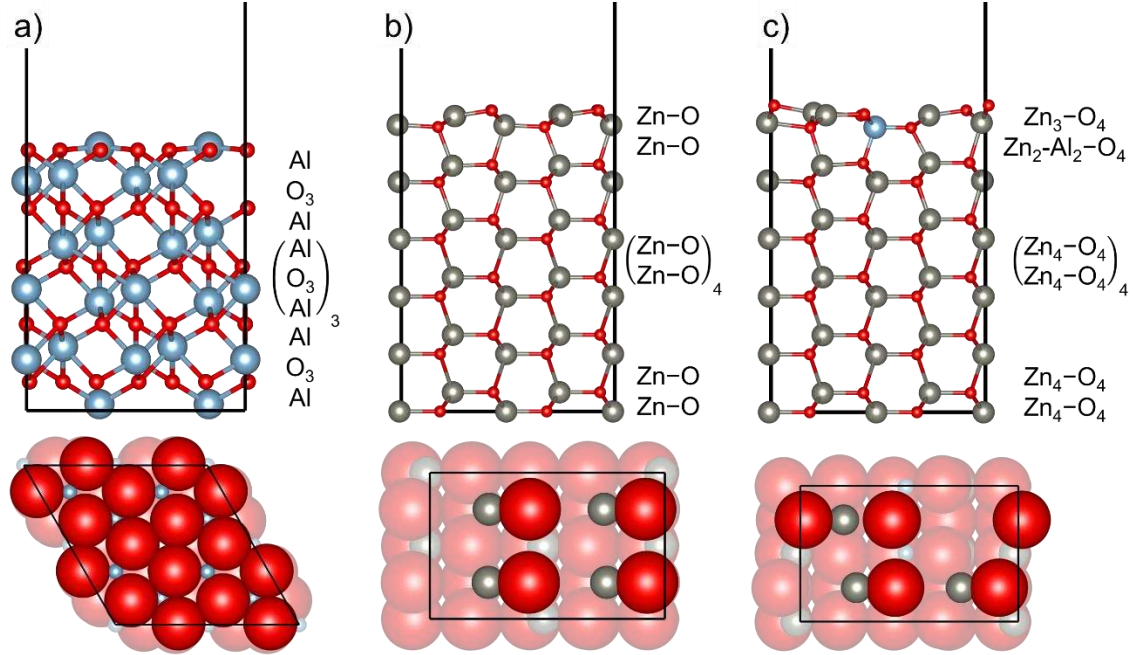


Fig. 7. Top and bottom panels represent the side and top projections of the optimised structures of (a) α - $\text{Al}_2\text{O}_3(0001)$ surface, (b) $\text{ZnO}(10\bar{1}0)$ surface and (c) $\text{Al}_2\text{O}_3/\text{ZnO}(10\bar{1}0)$ interface. The stacking of the atomic layers and the crystallographic directions are specified. The exposed planes containing ions with dangling bonds are emphasized in the top projection. O atoms are in red, Zn atoms are in grey and Al atoms are in blue.

The Al termination of the α - $\text{Al}_2\text{O}_3(0001)$ surface is a **Tasker** type 2 surface [23], whose exposed planes display a bulk-like structure consisting of 3-fold under-coordinated O anions decorated by 1/3 monolayer (ML) of 3-coordinated Al cations with 3 dangling bonds. Following relaxation of the Al-termination, we found that the protruding 3-fold Al ions moved inwards by 0.66 Å. The cations in the double **sub**-surface layers became closer by 0.23 Å, with the Al-4 layer moving outwards by 0.21 Å and the Al-3 plane migrating towards the bulk, showing 10% displacement of the deepest atoms. The under-coordinated O and the **sub**-surface O-5 layer moved towards the surface by 0.05 and 0.04 Å, respectively, as they prefer to lie as close as possible to the cations.

$\text{ZnO}(10\bar{1}0)$ is a Tasker **type 1** surface [23], composed of double stoichiometric stacking planes, which are separated by 0.94 and 1.88 Å, as displayed in Figure 7b. Creating the surface from the bulk of ZnO leads to a reduction in the coordination number of the exposed ions, *i.e.* Zn and O become 3-fold, compared to their 5-fold distorted square pyramidal coordination environment in the bulk [25,26]. Our calculations suggest that the

surface and sub-surface atoms move towards the bulk during geometry optimisation, with the largest shift of position of 0.55 Å obtained for the under-coordinated Zn. We found that the 3-fold O atoms moved by 49% of the shift observed for the cations of the same stoichiometric layer. However, the Zn atoms of the Zn–O-2 layer migrated by only 36% of the distance covered by the counteranions of the same stoichiometric unit, which was a modest 0.14 Å. Although less pronounced, the relaxation of the stoichiometric layers Zn–O-3 and Zn–O-4 showed similar behaviour to the Zn–O-1 and Zn–O-2, respectively. The Zn ions in the Zn–O-3 and Zn–O-4 layers moved towards the bulk by 0.16 and 0.02 Å, respectively, whereas the corresponding O anions migrated by 0.14 and 0.04 Å, respectively.

The most stable Al₂O₃/ZnO (10 $\bar{1}$ 0) interface was constructed by replacing two Zn ions from the Zn–O-2 layer by Al atoms and by creating a Zn vacancy in the layer of under-coordinated cations to ensure that the surface slab remained charge neutral, see Figure 7c [49]. Our calculations show that 2/3 of the 3-fold Zn ions migrated 0.03 Å inwards during geometry optimisation, whereas the remaining 1/3 of the exposed cations migrated outwards by 0.04 Å. The large Al atoms were displaced inwards by 0.17 Å with respect to the position originally occupied by the Zn cations in the relaxed pristine surface, whereas the remaining small Zn cations in the Zn–O-2 layer moved by 0.07 Å towards the surface. This pattern of relaxation led to half of the cations shifting towards the surface by 0.09 Å in the Zn–O-3 layer and the other half moving in the opposite direction, but only by 0.04 Å. This effect was reduced in the Zn–O-4 layer, where half of the Zn atoms moved inwards by 0.05 Å and the remaining cations migrated outwards by an average of 0.02 Å. The DFT calculations show that 75% of the under-coordinated O atoms moved towards the bulk by an average of 0.20 Å, and the other 25% shifted towards the surface by the same distance. However, we observed that the Zn–O-2, Zn–O-3 and Zn–O-4 layers migrated in alternating directions by 0.10, 0.04 and 0.02 Å, respectively.

The interfacial free energy (σ_{int}) was estimated as:

$$\sigma_{\text{int}} = \gamma_{\text{r}} + (E_{\text{int}} + n_{\text{ZnO}}E_{\text{ZnO}} - n_{\text{Al}_2\text{O}_3}E_{\text{Al}_2\text{O}_3})/A, \quad (6)$$

where E_{int} is the energy of the heterojunction; E_{ZnO} and $E_{\text{Al}_2\text{O}_3}$ are the bulk energies of one formula unit (f.u.) of ZnO and Al_2O_3 , respectively; and n_{ZnO} and $n_{\text{Al}_2\text{O}_3}$ represent the number of f.u.'s of ZnO removed and Al_2O_3 added, respectively, to form the interface.

From our calculations and previous works [21,26], we have determined that ZnO (10 $\bar{1}$ 0) is the most stable surface, whereas α - Al_2O_3 (0001) is the least stable system, as they have the lowest and highest surface energies (γ_r), respectively, see Table S1. We have used the Bader partition scheme [99–101] to calculate the atomic charges (q), which are slightly larger for the exposed cations of the parent materials and the interface than for the sub-surface cations. However, we found that the charge decreases upon formation of the heterojunction for Zn in the $\text{Zn}_3\text{-O}_4\text{-1}$ sheet and for Al in the $\text{Zn}_2\text{-Al}_2\text{-O}_4\text{-2}$ layer with respect to the same cations in the pristine surfaces. Our calculations suggest that this loss of charge is compensated by the increase of positive charge on Zn in the $\text{Zn}_2\text{-Al}_2\text{-O}_4\text{-2}$ plane and negative charge of the anions in both the exposed and sub-surface layers of the interface. The work function (Φ), which quantifies the energy needed to transfer the loosest held electron from the Fermi level (E_F) of the surface into the vacuum, was obtained by subtracting E_F to the potential of the vacuum (E_{vac}). Our simulations show that the formation of the interface reduces the work function of the sensor to 5.35 eV, which is the lowest value obtained in this work, thus explaining the larger sensitivity and reactivity of this system.

The framework of the Tersoff-Hamann methodology [102], as implemented in the HIVE program [103], was employed to simulate the scanning tunnelling microscopy images (STM), as used previously in the simulation of myriad materials [16,21,94,97,104,105]. The value of the sample bias employed for the calculation of the STM images characterises the surroundings of the Fermi level (E_F), *i.e.* the valence band maximum and the conduction band minimum. The negative bias used to calculate the STM profiles of the bare surfaces and the interface implies that the electrons located at the valence band move to the tip of the probe, which helps to resolve the exposed O ions as brighter spots than the cations. The images also show the exposed Al atoms in the α - Al_2O_3 (0001) surface, whereas the Zn atoms are difficult to identify in the ZnO (10 $\bar{1}$ 0) facet, see Figure 8a,b. However, the creation of the Zn vacancy in the exposed surface layer as well as the introduction of Al atoms in the sub-surface layer induces a charge reorganisation in

the $\text{Al}_2\text{O}_3/\text{ZnO}$ ($10\bar{1}0$) interface that leads to a better resolution of the cations in the STM image, see Figure 8c.

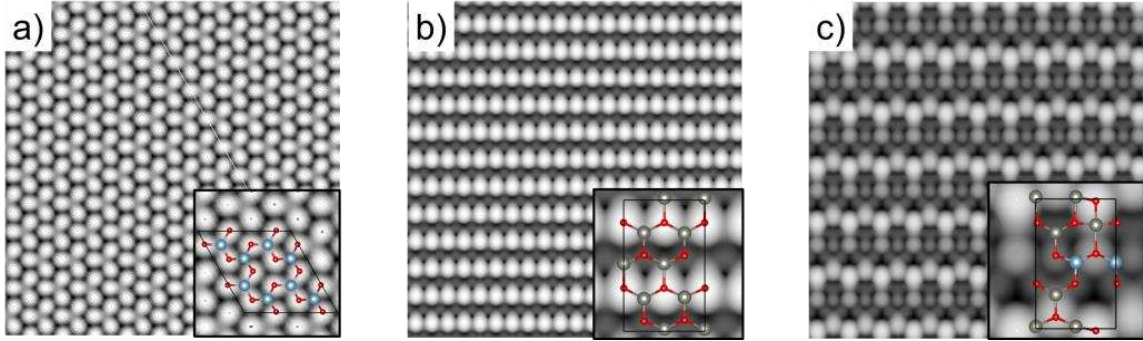


Fig. 8. Simulated scanning tunnelling microscopy (STM) profiles of (a) $\alpha\text{-Al}_2\text{O}_3(0001)$ facet, (b) $\text{ZnO}(10\bar{1}0)$ facet and (c) $\text{Al}_2\text{O}_3/\text{ZnO}(10\bar{1}0)$ interface. The bias used was (a) $V = -2.5$ eV, (b) $V = -2.0$ eV and (c) $V = -2.0$ eV; the density used was (a) $\rho = 0.0036$ e \AA^{-3} , (b) $\rho = 0.0040$ e \AA^{-3} and (c) $\rho = 0.0010$ e \AA^{-3} and the tip distance used was (a) $d = 1.50$ \AA , (b) $d = 2.00$ \AA and (c) $d = 2.40$ \AA . Crystallographic directions are specified. O atoms are in red, Zn atoms are in grey and Al atoms are in blue.

3.6 Adsorption of Molecules

We now provide a comparative and comprehensive discussion and analysis of the surface chemistry of the pristine $\alpha\text{-Al}_2\text{O}_3$ (0001) and $\text{ZnO}(10\bar{1}0)$ surfaces as well as the $\text{Al}_2\text{O}_3/\text{ZnO}(10\bar{1}0)$ heterojunction, where we have simulated the interaction with $\text{C}_3\text{H}_6\text{O}_2$, $\text{C}_4\text{H}_{10}\text{O}_2$, NO_2 and PF_5 , which are important components of lithium-ion batteries, as well as H_2O to assess the impact of humidity on the sensor. We have assumed that the battery electrolytes E1 and LP30, which respectively contain LiNO_3 and LiPF_6 as the main solutes, decompose and release the inorganic gases NO_2 [106] and PF_5 [107–109], respectively. We have investigated the binding configurations, where the negatively charged O and F atoms of the adsorbates coordinate the positively charged cations exposed at the surfaces of the sensors. Since the adsorption on the $\text{ZnO}(10\bar{1}0)$ surfaces provides a model of the uncoated sensor, we only considered the interaction with the Zn site closest to the Al dopant in the $\text{Al}_2\text{O}_3/\text{ZnO}(10\bar{1}0)$ interface system. The atoms forming the interactions were initially located at approximately 1.5 \AA above the surfaces before allowing the entire systems to relax fully to their thermodynamically stable

adsorption configurations, following the same approach used in our previous studies [24–26].

Table S2 displays the interaction energies (E_{ads}) for the adsorption of the adsorbates with the α -Al₂O₃ (0001), ZnO (10 $\bar{1}$ 0) and Al₂O₃/ZnO (10 $\bar{1}$ 0) surfaces. The largest adsorption energies were calculated for the interactions with the pristine α -Al₂O₃ (0001) surface, whereas the smallest binding energies were calculated for the ZnO (10 $\bar{1}$ 0) surface. The largest energy difference between the parent α -Al₂O₃ (0001) and ZnO (10 $\bar{1}$ 0) surfaces was calculated at 1.44 eV for PF₅ and the smallest binding energy difference at 0.16 eV was obtained for H₂O. The adsorption energies of the adsorbates are larger at the Zn than at the Al sites of the Al₂O₃/ZnO (10 $\bar{1}$ 0) heterojunction, and this preference increases from PF₅ to H₂O. The decreasing order of simulated adsorption energies on the most favourable Zn position of the Al₂O₃/ZnO (10 $\bar{1}$ 0) interface is $E_{\text{ads}}(\text{C}_3\text{H}_6\text{O}_2) > E_{\text{ads}}(\text{C}_4\text{H}_{10}\text{O}_2) \approx E_{\text{ads}}(\text{H}_2\text{O}) > E_{\text{ads}}(\text{NO}_2) > E_{\text{ads}}(\text{PF}_5)$. Importantly, the trend of the calculated adsorption energies suggests that humidity will not affect the detection of the volatile organic compounds. Our calculations reveal that overall the largest adsorption energy is released by PF₅ on the α -Al₂O₃ (0001) surface, whereas the binding energy of PF₅ is smallest on the ZnO (10 $\bar{1}$ 0) facet. The calculated adsorption energies for the components of the battery electrolyte at the Zn site of the Al₂O₃/ZnO (10 $\bar{1}$ 0) interface are in excellent agreement with our experimental investigation of the gas response. Our computations also describe the effect of growing the width of the Al₂O₃ overlayer leading to a reduction and an increase, respectively, of the selectivity towards C₃H₆O₂ and LP30, which is calculated as PF₅. The calculated charge transfers indicate that only NO₂ and PF₅ gained electron density upon adsorption at the α -Al₂O₃ (0001) and ZnO (10 $\bar{1}$ 0) surfaces, which were 20 times larger on the former than the latter. However, the largest charge donated by the organic adsorbates to the parent materials was observed at the ZnO (10 $\bar{1}$ 0) surface. All the gas molecules gained electron charge upon adsorption at the Al sites of the Al₂O₃/ZnO (10 $\bar{1}$ 0) interface, but only the organic adsorbates and H₂O donated electron density to the Zn positions.

We now discuss the geometries of the most stable interactions between the molecules and the Zn site of the Al₂O₃/ZnO (10 $\bar{1}$ 0) interface, which are displayed in Figure 9. As mentioned previously, the organic molecules show a preference for the heterojunction,

where we obtained distances between the surface Zn cations and the molecular O atoms of 2.04 and ~ 2.19 Å for the interactions with $C_4H_{10}O_2$ and $C_3H_6O_2$, respectively. We also found evidence that the ring of $C_3H_6O_2$ lies flat with respect to the surface, to allow its two O atoms to coordinate two nearby exposed Zn atoms, which explains the large adsorption energy of this molecule. However, only one of the O atoms of $C_4H_{10}O_2$ binds the Al_2O_3/ZnO ($10\bar{1}0$) surface, since its other O atom is not in a favourable position to coordinate another Zn atom. The NO_2 molecule forms a bidentate adsorption mode with the surface, where the O atoms of the adsorbate coordinate to Zn atoms at 2.02 and 2.11 Å. The largest distance of 2.58 Å was simulated for the least stable interaction of PF_5 , suggesting that this adsorbate remains weakly physisorbed to the surface, with negligible intramolecular changes with regard to the isolated species. Finally, the O atom of H_2O coordinates the Zn atom at 2.06 Å, whereas one of its H atoms forms a hydrogen bond to a nearby surface anion.

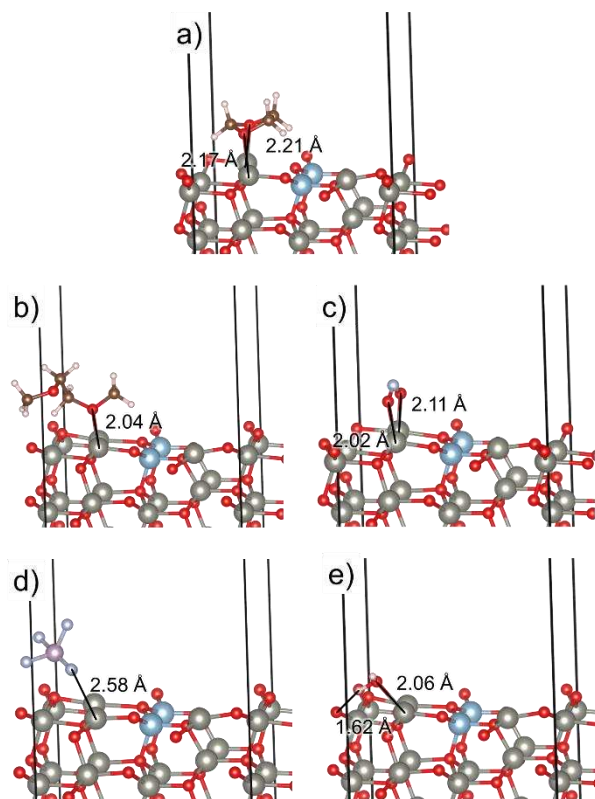


Fig. 9. Adsorption of (a) $C_3H_6O_2$, (b) $C_4H_{10}O_2$, (c) NO_2 , (d) PF_5 and (e) H_2O on the Zn site of the $Al_2O_3/ZnO(10\bar{1}0)$ surface. Interatomic distances are indicated and crystallographic directions are shown

with regard to the ZnO(10 $\bar{1}$ 0) substrate. O atoms are in red, H atoms are in white, C atoms are in brown, F atoms are in light blue, P atoms are in pink, Zn atoms are in grey and Al atoms are in blue.

4. Conclusions

We have investigated the effects of the chemical, structural, and morphological properties of Al₂O₃/ZnO heterostructures on their sensor characteristics. Gas detection studies have shown that Al₂O₃ coverage of ZnO is an effective procedure to enhance sensing for the electrolyte components of lithium-ion batteries. High C₃H₄O₁₀ vapor response and selectivity by the Al₂O₃/ZnO films were observed, with the highest response shown for the heterostructure with an Al₂O₃ layer thickness of 10 nm. We have also employed DFT methods to simulate the binding structures and energetics as well as electron charge transfers for the adsorption of a number of molecular species onto the pristine α -Al₂O₃ (0001) and ZnO (10 $\bar{1}$ 0) surfaces as well as the Al₂O₃/ZnO (10 $\bar{1}$ 0) interface, having first compared the structures and properties of the three systems. We calculated negative binding energies for the adsorption of all the molecular species with the surfaces and the heterojunction, suggesting that these are thermodynamically favourable and feasible processes. α -Al₂O₃ (0001) is the most reactive material, but the molecular adsorptions are more exothermic at the very exothermic Zn sites of the interface than at the Al sites. The analysis of the adsorption energies indicates that humidity will not affect the sensing properties towards the volatile organic compounds. The adsorbates gained electron density after coordinating the Al atom, but provided electron density for their interaction with the Zn position, lending support to the coordinate character of the molecular adsorption with the sensor. The decreasing order of preference for the interaction of the lithium-ion battery electrolyte species at the Zn site of the Al₂O₃/ZnO (10 $\bar{1}$ 0) interface is $E_{\text{ads}}(\text{C}_3\text{H}_6\text{O}_2) > E_{\text{ads}}(\text{C}_4\text{H}_{10}\text{O}_2) \approx E_{\text{ads}}(\text{H}_2\text{O}) > E_{\text{ads}}(\text{NO}_2) > E_{\text{ads}}(\text{PF}_5)$. Thus, this novel sensor type is ideal for lithium-sulfur batteries as they are highly sensitive to the used solvents, compared to other sensor types available.

Acknowledgements

We acknowledge funding within the project “SuSiBaBy” - SulfurSilicon Batteries by the EUSH and EFRE in SH (LPW-E/3.1.1/1801). We are especially grateful to the Federal

Ministry of Education and Research by funding the former “PorSSi” project (03XP0126 A & B). *Via* our membership of the UK's HEC Materials Chemistry Consortium, which is funded by EPSRC (EP/R029431), this work used the ARCHER UK National Supercomputing Service (<http://www.archer.ac.uk>). This research has also used the Supercomputing Facilities at Cardiff University operated by the Advanced Research Computing @ Cardiff (ARCCA) Division on behalf of the Supercomputing Wales (SCW) project, which is part-funded by the European Regional Development Fund (ERDF) *via* the Welsh Government. Finally, we have carried out calculations on ARC4, part of the High-Performance Computing facilities at the University of Leeds, United Kingdom. All data created during this research is provided in full in the results section of this paper.

References

- [1] M. Armand, J.-M. Tarascon, Building better batteries, *Nature*. 451 (2008) 652–657. <https://doi.org/10.1038/451652a>.
- [2] A. Manthiram, An outlook on lithium ion battery technology, *ACS Cent. Sci.* 3 (2017) 1063–1069. <https://doi.org/10.1021/acscentsci.7b00288>.
- [3] J.B. Goodenough, K.-S. Park, The Li-Ion rechargeable battery: A Perspective, *J. Am. Chem. Soc.* 135 (2013) 1167–1176. <https://doi.org/10.1021/ja3091438>.
- [4] B. Sundén, Battery technologies, in: B. Sundén (Ed.), *Hydrogen, Batteries and Fuel Cells*, Elsevier, 2019, pp. 57–79. <https://doi.org/10.1016/B978-0-12-816950-6.00004-X>.
- [5] Y. Chen, Y. Kang, Y. Zhao, L. Wang, J. Liu, Y. Li, Z. Liang, X. He, X. Li, N. Tavajohi, B. Li, A review of lithium-ion battery safety concerns: The issues, strategies, and testing standards, *J. Energy Chem.* 59 (2021) 83–99. <https://doi.org/10.1016/j.jechem.2020.10.017>.
- [6] G.E. Blomgren, The development and future of lithium ion batteries, *J. Electrochem. Soc.* 164 (2017) A5019–A5025. <https://doi.org/10.1149/2.0251701jes>.
- [7] The journey of an electrifying (r)evolution, *Nat. Commun.* 12 (2021) 4153. <https://doi.org/10.1038/s41467-021-24410-3>.
- [8] Technologies of energy storage systems, in: F.-B. Wu, B. Yang, J.-L. Ye, (Eds.), *Grid-scale Energy Storage Systems and Applications*, Elsevier, 2019, pp. 17–56. <https://doi.org/10.1016/B978-0-12-815292-8.00002-2>.
- [9] P. Kurzweil, Post-lithium-ion battery chemistries for hybrid electric vehicles and battery electric vehicles, in: B. Scrosati, J. Garche, W. Tillmetz (Eds.), *Advances in Battery Technologies for Electric Vehicles*, Elsevier, 2015, pp. 127–172. <https://doi.org/10.1016/B978-1-78242-377-5.00007-8>.
- [10] H.-J. Peng, J.-Q. Huang, X.-B. Cheng, Q. Zhang, Review on high-loading and high-energy lithium-sulfur batteries, *Adv. Energy Mater.* 7 (2017) 1700260. <https://doi.org/10.1002/aenm.201700260>.
- [11] D.H. Doughty, E.P. Roth, A general discussion of Li ion battery safety, *Electrochem. Soc. Interface.* 21 (2012) 37–44. <https://doi.org/10.1149/2.F03122if>.

- [12] Z. Wang, L. Zhu, J. Liu, J. Wang, W. Yan, Gas sensing technology for the detection and early warning of battery thermal runaway: a review, *Energy & Fuels*. 36 (2022) 6038–6057. <https://doi.org/10.1021/acs.energyfuels.2c01121>.
- [13] S. Koch, K. Birke, R. Kuhn, Fast thermal runaway detection for lithium-ion cells in large scale traction batteries, *Batteries*. 4 (2018) 16. <https://doi.org/10.3390/batteries4020016>.
- [14] C. Essl, L. Seifert, M. Rabe, A. Fuchs, Early detection of failing automotive batteries using gas sensors, *Batteries*. 7 (2021) 25. <https://doi.org/10.3390/batteries7020025>.
- [15] O. Lupan, N. Ababii, A.K. Mishra, M.T. Bodduluri, N. Magariu, A. Vahl, H. Krüger, B. Wagner, F. Faupel, R. Adelung, N.H. de Leeuw, S. Hansen, Heterostructure-based devices with enhanced humidity stability for H₂ gas sensing applications in breath tests and portable batteries, *Sensors Actuators A Phys*. 329 (2021) 112804. <https://doi.org/10.1016/j.sna.2021.112804>.
- [16] O. Lupan, D. Santos-Carballal, N. Ababii, N. Magariu, S. Hansen, A. Vahl, L. Zimoch, M. Hoppe, T. Pauporté, V. Galstyan, V. Sontea, L. Chow, F. Faupel, R. Adelung, N.H. de Leeuw, E. Comini, TiO₂/Cu₂O/CuO multi-nanolayers as sensors for H₂ and volatile organic compounds: an experimental and theoretical investigation, *ACS Appl. Mater. Interfaces*. 13 (2021) 32363–32380. <https://doi.org/10.1021/acsami.1c04379>.
- [17] O.A. Dicks, A.L. Shluger, Theoretical modeling of charge trapping in crystalline and amorphous Al₂O₃, *J. Phys. Condens. Matter*. 29 (2017) 314005. <https://doi.org/10.1088/1361-648X/aa7767>.
- [18] S. Davis, G. Gutiérrez, Structural, elastic, vibrational and electronic properties of amorphous Al₂O₃ from ab initio calculations, *J. Phys. Condens. Matter*. 23 (2011) 495401. <https://doi.org/10.1088/0953-8984/23/49/495401>.
- [19] R. Lizárraga, E. Holmström, S.C. Parker, C. Arrouvel, Structural characterization of amorphous alumina and its polymorphs from first-principles XPS and NMR calculations, *Phys. Rev. B*. 83 (2011) 094201. <https://doi.org/10.1103/PhysRevB.83.094201>.
- [20] M. Liu, Y. Jin, C. Leygraf, J. Pan, A DFT-study of Cl ingress into α -Al₂O₃ (0001)

- and Al(111) and its possible influence on localized corrosion of Al, *J. Electrochem. Soc.* 166 (2019) C3124–C3130. <https://doi.org/10.1149/2.0161911jes>.
- [21] B. Ramogayana, D. Santos-Carballal, K.P. Maenetja, N.H. de Leeuw, P.E. Ngoepe, Density functional theory study of ethylene carbonate adsorption on the (0001) surface of aluminum oxide α -Al₂O₃, *ACS Omega*. 6 (2021) 29577–29587. <https://doi.org/10.1021/acsomega.1c03771>.
- [22] N. Sharifi, C. Falamaki, M.G. Ahangari, DFT study of Au adsorption on pure and Pt-decorated γ -alumina (110) surface, *Appl. Surf. Sci.* 416 (2017) 390–396. <https://doi.org/10.1016/j.apsusc.2017.04.203>.
- [23] P.W. Tasker, The stability of ionic crystal surfaces, *J. Phys. C Solid State Phys.* 12 (1979) 4977–4984. <https://doi.org/10.1088/0022-3719/12/22/036>.
- [24] V. Postica, A. Vahl, D. Santos-Carballal, T. Dankwort, L. Kienle, M. Hoppe, A. Cadi-Essadek, N.H. de Leeuw, M.-I. Terasa, R. Adelung, F. Faupel, O. Lupan, Tuning ZnO sensors reactivity toward volatile organic compounds via Ag doping and nanoparticle functionalization, *ACS Appl. Mater. Interfaces*. 11 (2019) 31452–31466. <https://doi.org/10.1021/acsomega.9b07275>.
- [25] A. Vahl, O. Lupan, D. Santos-Carballal, V. Postica, S. Hansen, H. Cavers, N. Wolff, M.-I. Terasa, M. Hoppe, A. Cadi-Essadek, T. Dankwort, L. Kienle, N.H. de Leeuw, R. Adelung, F. Faupel, Surface functionalization of ZnO:Ag columnar thin films with AgAu and AgPt bimetallic alloy nanoparticles as an efficient pathway for highly sensitive gas discrimination and early hazard detection in batteries, *J. Mater. Chem. A*. 8 (2020) 16246–16264. <https://doi.org/10.1039/D0TA03224G>.
- [26] V. Postica, A. Vahl, J. Strobel, D. Santos-Carballal, O. Lupan, A. Cadi-Essadek, N.H. De Leeuw, F. Schütt, O. Polonskyi, T. Strunskus, M. Baum, L. Kienle, R. Adelung, F. Faupel, Tuning doping and surface functionalization of columnar oxide films for volatile organic compounds sensing: experiments and theory, *J. Mater. Chem. A*. 6 (2018) 23669–23682. <https://doi.org/10.1039/C8TA08985J>.
- [27] O. Lupan, L. Chow, S. Shishiyanu, E. Monaico, T. Shishiyanu, V. Şontea, B. Roldan Cuenya, A. Naitabdi, S. Park, A. Schulte, Nanostructured zinc oxide films synthesized by successive chemical solution deposition for gas sensor applications, *Mater. Res. Bull.* 44 (2009) 63–69.

<https://doi.org/10.1016/j.materresbull.2008.04.006>.

- [28] O. Lupan, S. Shishiyanu, L. Chow, T. Shishiyanu, Nanostructured zinc oxide gas sensors by successive ionic layer adsorption and reaction method and rapid photothermal processing, *Thin Solid Films*. 516 (2008) 3338–3345. <https://doi.org/10.1016/j.tsf.2007.10.104>.
- [29] G. Kresse, J. Hafner, Ab initio molecular dynamics for liquid metals, *Phys. Rev. B*. 47 (1993) 558–561. <https://doi.org/10.1103/PhysRevB.47.558>.
- [30] G. Kresse, J. Hafner, Ab initio molecular-dynamics simulation of the liquid-metal–amorphous-semiconductor transition in germanium, *Phys. Rev. B*. 49 (1994) 14251–14269. <https://doi.org/10.1103/PhysRevB.49.14251>.
- [31] G. Kresse, J. Furthmüller, Efficient iterative schemes for ab initio total-energy calculations using a plane-wave basis set, *Phys. Rev. B*. 54 (1996) 11169–11186. <https://doi.org/10.1103/PhysRevB.54.11169>.
- [32] G. Kresse, J. Furthmüller, Efficiency of ab-initio total energy calculations for metals and semiconductors using a plane-wave basis set, *Comput. Mater. Sci*. 6 (1996) 15–50. [https://doi.org/10.1016/0927-0256\(96\)00008-0](https://doi.org/10.1016/0927-0256(96)00008-0).
- [33] J.P. Perdew, K. Burke, M. Ernzerhof, Generalized gradient approximation made simple [*Phys. Rev. Lett.* 77, 3865 (1996)], *Phys. Rev. Lett.* 78 (1997) 1396–1396. <https://doi.org/10.1103/PhysRevLett.78.1396>.
- [34] J.P. Perdew, K. Burke, M. Ernzerhof, Generalized gradient approximation made simple, *Phys. Rev. Lett.* 77 (1996) 3865–3868. <https://doi.org/10.1103/PhysRevLett.77.3865>.
- [35] S. Grimme, J. Antony, S. Ehrlich, H. Krieg, A consistent and accurate ab initio parametrization of density functional dispersion correction (DFT-D) for the 94 elements H-Pu, *J. Chem. Phys.* 132 (2010) 154104. <https://doi.org/10.1063/1.3382344>.
- [36] S. Grimme, S. Ehrlich, L. Goerigk, Effect of the damping function in dispersion corrected density functional theory, *J. Comput. Chem.* 32 (2011) 1456–1465. <https://doi.org/10.1002/jcc.21759>.
- [37] D. Santos-Carballeda, A. Cadi-Essadek, N.H. de Leeuw, Catalytic conversion of CO and H₂ into hydrocarbons on the cobalt Co(111) surface: implications for the

- fischer–tropsch process, *J. Phys. Chem. C.* 125 (2021) 11891–11903. <https://doi.org/10.1021/acs.jpcc.1c00254>.
- [38] A. Cadi-Essadek, A. Roldan, D. Santos-Carballal, P.E. Ngoepe, M. Claeys, N.H. de Leeuw, DFT+U study of the electronic, magnetic and mechanical properties of Co, CoO, and Co₃O₄, *South African J. Chem.* 74 (2021) 8–16. <https://doi.org/10.17159/0379-4350/2021/v74a3>.
- [39] L.M. Botha, D. Santos-Carballal, U. Terranova, M.G. Quesne, M.J. Ungerer, C.G.C.E. van Sittert, N.H. de Leeuw, Mixing thermodynamics and electronic structure of the Pt_{1-x}Ni_x (0 ≤ x ≤ 1) bimetallic alloy, *RSC Adv.* 9 (2019) 16948–16954. <https://doi.org/10.1039/C9RA02320H>.
- [40] B. Ramogayana, D. Santos-Carballal, P.A. Aparicio, M.G. Quesne, K.P. Maenetja, P.E. Ngoepe, N.H. de Leeuw, Ethylene carbonate adsorption on the major surfaces of lithium manganese oxide Li_{1-x}Mn₂O₄ spinel (0.000 < x < 0.375): a DFT+U–D3 study, *Phys. Chem. Chem. Phys.* 22 (2020) 6763–6771. <https://doi.org/10.1039/C9CP05658K>.
- [41] L. Reguera, N.L. López, J. Rodríguez-Hernández, M. González, C.E. Hernandez-Tamargo, D. Santos-Carballal, N.H. de Leeuw, E. Reguera, Synthesis, crystal structures, and properties of zeolite-like T₃(H₃O)₂M(CN)₆]₂·uH₂O (T = Co, Zn; M = Ru, Os), *Eur. J. Inorg. Chem.* 2017 (2017) 2980–2989. <https://doi.org/10.1002/ejic.201700278>.
- [42] P.E. Blöchl, Projector augmented-wave method, *Phys. Rev. B.* 50 (1994) 17953–17979. <https://doi.org/10.1103/PhysRevB.50.17953>.
- [43] G. Kresse, D. Joubert, From ultrasoft pseudopotentials to the projector augmented-wave method, *Phys. Rev. B.* 59 (1999) 1758–1775. <https://doi.org/10.1103/PhysRevB.59.1758>.
- [44] D. Sheppard, R. Terrell, G. Henkelman, Optimization methods for finding minimum energy paths, *J. Chem. Phys.* 128 (2008) 134106. <https://doi.org/10.1063/1.2841941>.
- [45] E. Bitzek, P. Koskinen, F. Gähler, M. Moseler, P. Gumbsch, Structural relaxation made simple, *Phys. Rev. Lett.* 97 (2006) 170201. <https://doi.org/10.1103/PhysRevLett.97.170201>.

- [46] S.L. Dudarev, G.A. Botton, S.Y. Savrasov, C.J. Humphreys, A.P. Sutton, Electron-energy-loss spectra and the structural stability of nickel oxide: an LSDA+U study, *Phys. Rev. B.* 57 (1998) 1505–1509. <https://doi.org/10.1103/PhysRevB.57.1505>.
- [47] V.I. Anisimov, M.A. Korotin, J. Zaanen, O.K. Andersen, Spin bags, polarons, and impurity potentials in $\text{La}_{2-x}\text{Sr}_x\text{CuO}_4$ from first principles, *Phys. Rev. Lett.* 68 (1992) 345–348. <https://doi.org/10.1103/PhysRevLett.68.345>.
- [48] H.J. Monkhorst, J.D. Pack, Special points for Brillouin-zone integrations, *Phys. Rev. B.* 13 (1976) 5188–5192. <https://doi.org/10.1103/PhysRevB.13.5188>.
- [49] O. Lupan, D. Santos-Carballal, N. Magariu, A.K. Mishra, N. Ababii, H. Krüger, N. Wolff, A. Vahl, M.T. Bodduluri, N. Kohlmann, L. Kienle, R. Adelung, N.H. de Leeuw, S. Hansen, $\text{Al}_2\text{O}_3/\text{ZnO}$ heterostructure-based sensors for volatile organic compounds in safety applications, *ACS Appl. Mater. Interfaces.* 14 (2022) 29331–29344. <https://doi.org/10.1021/acsami.2c03704>.
- [50] K.M. Ho, C.L. Fu, B.N. Harmon, W. Weber, D.R. Hamann, Vibrational frequencies and structural properties of transition metals via total-energy calculations, *Phys. Rev. Lett.* 49 (1982) 673–676. <https://doi.org/10.1103/PhysRevLett.49.673>.
- [51] C.L. Fu, K.M. Ho, First-principles calculation of the equilibrium ground-state properties of transition metals: applications to Nb and Mo, *Phys. Rev. B.* 28 (1983) 5480–5486. <https://doi.org/10.1103/PhysRevB.28.5480>.
- [52] M.S. Methfessel, M.H. Boon, F.M. Mueller, Analytic-quadratic method of calculating the density of states, *J. Phys. C Solid State Phys.* 16 (1983) L949–L954. <https://doi.org/10.1088/0022-3719/16/27/002>.
- [53] G. Lehmann, M. Taut, On the numerical calculation of the density of states and related properties, *Phys. Status Solidi.* 54 (1972) 469–477. <https://doi.org/10.1002/pssb.2220540211>.
- [54] O. Jepsen, O.K. Anderson, The electronic structure of h.c.p. Ytterbium, *Solid State Commun.* 9 (1971) 1763–1767. [https://doi.org/10.1016/0038-1098\(71\)90313-9](https://doi.org/10.1016/0038-1098(71)90313-9).
- [55] G. Gilat, Analysis of methods for calculating spectral properties in solids, *J. Comput. Phys.* 10 (1972) 432–465. [https://doi.org/10.1016/0021-9991\(72\)90046-0](https://doi.org/10.1016/0021-9991(72)90046-0).
- [56] P.E. Blöchl, O. Jepsen, O.K. Andersen, Improved tetrahedron method for

- Brillouin-zone integrations, *Phys. Rev. B.* 49 (1994) 16223–16233. <https://doi.org/10.1103/PhysRevB.49.16223>.
- [57] I. Rutkowska, J. Marchewka, P. Jeleń, M. Odziomek, M. Korpyś, J. Paczkowska, M. Sitarz, Chemical and structural characterization of amorphous and crystalline alumina obtained by alternative sol–gel preparation routes, *Materials.* 14 (2021) 1761. <https://doi.org/10.3390/ma14071761>.
- [58] F. Decremps, J. Pellicer-Porres, A.M. Saitta, J.-C. Chervin, A. Polian, High-pressure Raman spectroscopy study of wurtzite ZnO, *Phys. Rev. B.* 65 (2002) 092101. <https://doi.org/10.1103/PhysRevB.65.092101>.
- [59] M. Hoppe, O. Lupan, V. Postica, N. Wolff, V. Duppel, L. Kienle, I. Tiginyanu, R. Adelung, ZnAl₂O₄ -functionalized zinc oxide microstructures for highly selective hydrogen gas sensing applications, *Phys. Status Solidi.* 215 (2018) 1700772. <https://doi.org/10.1002/pssa.201700772>.
- [60] R.S. Zeferino, M.B. Flores, U. Pal, Photoluminescence and Raman scattering in Ag-doped ZnO nanoparticles, *J. Appl. Phys.* 109 (2011) 014308. <https://doi.org/10.1063/1.3530631>.
- [61] R. Cuscó, E. Alarcón-Lladó, J. Ibáñez, L. Artús, J. Jiménez, B. Wang, M.J. Callahan, Temperature dependence of Raman scattering in ZnO, *Phys. Rev. B.* 75 (2007) 165202. <https://doi.org/10.1103/PhysRevB.75.165202>.
- [62] V. Postica, I. Hölken, V. Schneider, V. Kaidas, O. Polonskyi, V. Cretu, I. Tiginyanu, F. Faupel, R. Adelung, O. Lupan, Multifunctional device based on ZnO:Fe nanostructured films with enhanced UV and ultra-fast ethanol vapour sensing, *Mater. Sci. Semicond. Process.* 49 (2016) 20–33. <https://doi.org/10.1016/j.mssp.2016.03.024>.
- [63] P.G. Li, M. Lei, W.H. Tang, Raman and photoluminescence properties of α -Al₂O₃ microcones with hierarchical and repetitive superstructure, *Mater. Lett.* 64 (2010) 161–163. <https://doi.org/10.1016/j.matlet.2009.10.032>.
- [64] D. Zappa, V. Galstyan, N. Kaur, H.M.M. Munasinghe Arachchige, O. Sisman, E. Comini, “Metal oxide -based heterostructures for gas sensors”- a review, *Anal. Chim. Acta.* 1039 (2018) 1–23. <https://doi.org/10.1016/j.aca.2018.09.020>.
- [65] M. Mathew, P. V Shinde, R. Samal, C.S. Rout, A review on mechanisms and

- recent developments in p-n heterojunctions of 2D materials for gas sensing applications, *J. Mater. Sci.* 56 (2021) 9575–9604. <https://doi.org/10.1007/s10853-021-05884-4>.
- [66] C. Marichy, N. Pinna, Atomic layer deposition to materials for gas sensing applications, *Adv. Mater. Interfaces.* 3 (2016) 1600335. <https://doi.org/10.1002/admi.201600335>.
- [67] Q. Yue, Z. Shao, S. Chang, J. Li, Adsorption of gas molecules on monolayer MoS₂ and effect of applied electric field, *Nanoscale Res Lett.* 8 (2013) 425. <https://doi.org/10.1186/1556-276X-8-425>.
- [68] J. Bai, C. Zhao, H. Gong, Q. Wang, B. Huang, G. Sun, Y. Wang, J. Zhou, E. Xie, F. Wang, Debye-length controlled gas sensing performances in NiO@ZnO p-n junctional core-shell nanotubes, *J. Phys. D. Appl. Phys.* 52 (2019) 285103. <https://doi.org/10.1088/1361-6463/ab182f>.
- [69] A. Rosental, A. Tarre, A. Gerst, J. Sundqvist, A. Hårsta, A. Aidla, J. Aarik, V. Sammelselg, T. Uustare, Gas sensing properties of epitaxial SnO₂ thin films prepared by atomic layer deposition, *Sensors Actuators B Chem.* 93 (2003) 552–555. [https://doi.org/10.1016/S0925-4005\(03\)00236-3](https://doi.org/10.1016/S0925-4005(03)00236-3).
- [70] N.A. Yebo, S.P. Sree, E. Levrau, C. Detavernier, Z. Hens, J.A. Martens, R. Baets, Selective and reversible ammonia gas detection with nanoporous film functionalized silicon photonic micro-ring resonator, *Opt. Express.* 20 (2012) 11855. <https://doi.org/10.1364/OE.20.011855>.
- [71] D.-H. Kim, W.-S. Kim, S. Kim, S.-H. Hong, Brookite TiO₂ thin film epitaxially grown on (110) YSZ substrate by atomic layer deposition, *ACS Appl. Mater. Interfaces.* 6 (2014) 11817–11822. <https://doi.org/10.1021/am501656r>.
- [72] I. Levin, D. Brandon, Metastable alumina polymorphs: crystal structures and transition sequences, *J. Am. Ceram. Soc.* 81 (2005) 1995–2012. <https://doi.org/10.1111/j.1151-2916.1998.tb02581.x>.
- [73] Y. Zou, S. Xi, T. Bo, X. Zhou, J. Ma, X. Yang, C. Diao, Y. Deng, Mesoporous amorphous Al₂O₃/crystalline WO₃ heterophase hybrids for electrocatalysis and gas sensing applications, *J. Mater. Chem. A.* 7 (2019) 21874–21883. <https://doi.org/10.1039/C9TA08633A>.

- [74] Y.K. Mishra, G. Modi, V. Cretu, V. Postica, O. Lupan, T. Reimer, I. Paulowicz, V. Hrkac, W. Benecke, L. Kienle, R. Adelung, Direct growth of freestanding ZnO tetrapod networks for multifunctional applications in photocatalysis, UV photodetection, and gas sensing, *ACS Appl. Mater. Interfaces*. 7 (2015) 14303–14316. <https://doi.org/10.1021/acsami.5b02816>.
- [75] D.R. Patil, L.A. Patil, D.P. Amalnerkar, Ethanol gas sensing properties of Al₂O₃-doped ZnO thick film resistors, *Bull. Mater. Sci.* 30 (2007) 553–559. <https://doi.org/10.1007/s12034-007-0086-6>.
- [76] C.H. Kwon, H.-K. Hong, D.H. Yun, K. Lee, S.-T. Kim, Y.-H. Roh, B.-H. Lee, Thick-film zinc-oxide gas sensor for the control of lean air-to-fuel ratio in domestic combustion systems, *Sensors Actuators B Chem.* 25 (1995) 610–613. [https://doi.org/10.1016/0925-4005\(95\)85134-8](https://doi.org/10.1016/0925-4005(95)85134-8).
- [77] V. V. Kondalkar, L.T. Duy, H. Seo, K. Lee, Nanohybrids of Pt-functionalized Al₂O₃/ZnO core-shell nanorods for high-performance MEMS-based acetylene gas sensor, *ACS Appl. Mater. Interfaces*. 11 (2019) 25891–25900. <https://doi.org/10.1021/acsami.9b06338>.
- [78] Y. Zhu, Y. Zhao, J. Ma, X. Cheng, J. Xie, P. Xu, H. Liu, H. Liu, H. Zhang, M. Wu, A.A. Elzatahry, A. Alghamdi, Y. Deng, D. Zhao, Mesoporous tungsten oxides with crystalline framework for highly sensitive and selective detection of foodborne pathogens, *J. Am. Chem. Soc.* 139 (2017) 10365–10373. <https://doi.org/10.1021/jacs.7b04221>.
- [79] Y. Li, W. Luo, N. Qin, J. Dong, J. Wei, W. Li, S. Feng, J. Chen, J. Xu, A.A. Elzatahry, M.H. Es-Saheb, Y. Deng, D. Zhao, Highly ordered mesoporous tungsten oxides with a large pore size and crystalline framework for H₂S sensing, *Angew. Chemie Int. Ed.* 53 (2014) 9035–9040. <https://doi.org/10.1002/anie.201403817>.
- [80] Q.-H. Xu, D.-M. Xu, M.-Y. Guan, Y. Guo, Q. Qi, G.-D. Li, ZnO/Al₂O₃/CeO₂ composite with enhanced gas sensing performance, *Sensors Actuators B Chem.* 177 (2013) 1134–1141. <https://doi.org/10.1016/j.snb.2012.12.029>.
- [81] I. Kocemba, M. Wrobeljedrzejewska, A. Szychowska, J. Rynkowski, M. Glowka, The properties of barium stannate and aluminum oxide-based gas sensor: the role

- of Al₂O₃ in this system, *Sensors Actuators B Chem.* 121 (2007) 401–405. <https://doi.org/10.1016/j.snb.2006.03.052>.
- [82] J. Wang, S. Jiang, H. Liu, S. Wang, Q. Pan, Y. Yin, G. Zhang, P- type gas-sensing behavior of Ga₂O₃/Al₂O₃ nanocomposite with high sensitivity to NO_x at room temperature, *J. Alloys Compd.* 814 (2020) 152284. <https://doi.org/10.1016/j.jallcom.2019.152284>.
- [83] S. Schröder, N. Ababii, O. Lupan, J. Drewes, N. Magariu, H. Krüger, T. Strunskus, R. Adelung, S. Hansen, F. Faupel, Sensing performance of CuO/Cu₂O/ZnO:Fe heterostructure coated with thermally stable ultrathin hydrophobic PV3D3 polymer layer for battery application, *Mater. Today Chem.* 23 (2022) 100642. <https://doi.org/10.1016/j.mtchem.2021.100642>.
- [84] A. Wildenberg, Y. Fenard, M. Carbonnier, A. Kéromnès, B. Lefort, Z. Serinyel, G. Dayma, L. Le Moyne, P. Dagaut, K.A. Heufer, An experimental and kinetic modeling study on the oxidation of 1,3-dioxolane, *Proc. Combust. Inst.* 38 (2021) 543–553. <https://doi.org/10.1016/j.proci.2020.06.362>.
- [85] A.H. Cutler, M.J. Antal, M. Jones, Kinetics and mechanism of the vapor phase pyrolysis of 1,3-dioxolane in steam, *J. Anal. Appl. Pyrolysis.* 12 (1987) 223–242. [https://doi.org/10.1016/0165-2370\(87\)85003-9](https://doi.org/10.1016/0165-2370(87)85003-9).
- [86] J.-H. Lee, J.-H. Kim, S.S. Kim, CuO–TiO₂ p–n core–shell nanowires: sensing mechanism and p/n sensing-type transition, *Appl. Surf. Sci.* 448 (2018) 489–497. <https://doi.org/10.1016/j.apsusc.2018.04.115>.
- [87] A. Mirzaei, J.-H. Kim, H.W. Kim, S.S. Kim, How shell thickness can affect the gas sensing properties of nanostructured materials: survey of literature, *Sensors Actuators B Chem.* 258 (2018) 270–294. <https://doi.org/10.1016/j.snb.2017.11.066>.
- [88] J.-H. Kim, A. Katoch, S.S. Kim, Optimum shell thickness and underlying sensing mechanism in p–n CuO–ZnO core–shell nanowires, *Sensors Actuators B Chem.* 222 (2016) 249–256. <https://doi.org/10.1016/j.snb.2015.08.062>.
- [89] N. Yamazoe, New approaches for improving semiconductor gas sensors, *Sensors Actuators B Chem.* 5 (1991) 7–19. [https://doi.org/10.1016/0925-4005\(91\)80213-4](https://doi.org/10.1016/0925-4005(91)80213-4).
- [90] G.W. Watson, E.T. Kelsey, N.H. de Leeuw, D.J. Harris, S.C. Parker, Atomistic simulation of dislocations, surfaces and interfaces in MgO, *J. Chem. Soc. Faraday*

- Trans. 92 (1996) 433–438. <https://doi.org/10.1039/ft9969200433>.
- [91] G. Makov, M.C. Payne, Periodic boundary conditions in ab initio calculations, *Phys. Rev. B.* 51 (1995) 4014–4022. <https://doi.org/10.1103/PhysRevB.51.4014>.
- [92] J. Neugebauer, M. Scheffler, Adsorbate-substrate and adsorbate-adsorbate interactions of Na and K adlayers on Al(111), *Phys. Rev. B.* 46 (1992) 16067–16080. <https://doi.org/10.1103/PhysRevB.46.16067>.
- [93] M.A. Peck, D. Santos-Carballal, N.H. de Leeuw, M. Claeys, Density functional theory study of the adsorption of oxygen and hydrogen on 3d transition metal surfaces with varying magnetic ordering, *South African J. Chem.* 74 (2021) 69–72. <https://doi.org/10.17159/0379-4350/2021/v74a11>.
- [94] D. Santos-Carballal, A. Roldan, R. Grau-Crespo, N.H. de Leeuw, A DFT study of the structures, stabilities and redox behaviour of the major surfaces of magnetite Fe_3O_4 , *Phys. Chem. Chem. Phys.* 16 (2014) 21082–21097. <https://doi.org/10.1039/c4cp00529e>.
- [95] C.E. Mitchell, D. Santos-Carballal, A.M. Beale, W. Jones, D.J. Morgan, M. Sankar, N.H. de Leeuw, The role of surface oxidation and Fe–Ni synergy in Fe–Ni–S catalysts for CO_2 hydrogenation, *Faraday Discuss.* 230 (2021) 30–51. <https://doi.org/10.1039/D0FD00137F>.
- [96] D. Santos-Carballal, A. Roldan, N.Y. Dzade, N.H. de Leeuw, Reactivity of CO_2 on the surfaces of magnetite (Fe_3O_4), greigite (Fe_3S_4) and mackinawite (FeS), *Philos. Trans. R. Soc. A Math. Phys. Eng. Sci.* 376 (2018) 20170065. <https://doi.org/10.1098/rsta.2017.0065>.
- [97] A.E. Shields, D. Santos-Carballal, N.H. de Leeuw, A density functional theory study of uranium-doped thoria and uranium adatoms on the major surfaces of thorium dioxide, *J. Nucl. Mater.* 473 (2016) 99–111. <https://doi.org/10.1016/j.jnucmat.2016.02.009>.
- [98] M.U. Ungerer, D. Santos-Carballal, C.G. van Sittert, N.H. de Leeuw, Competitive adsorption of H_2O and SO_2 on catalytic platinum surfaces: a density functional theory study, *South African J. Chem.* 74 (2021) 57–68. <https://doi.org/10.17159/0379-4350/2021/v74a10>.
- [99] G. Henkelman, A. Arnaldsson, H. Jónsson, A fast and robust algorithm for Bader

- decomposition of charge density, *Comput. Mater. Sci.* 36 (2006) 354–360. <https://doi.org/10.1016/j.commatsci.2005.04.010>.
- [100] E. Sanville, S.D. Kenny, R. Smith, G. Henkelman, Improved grid-based algorithm for Bader charge allocation, *J. Comput. Chem.* 28 (2007) 899–908. <https://doi.org/10.1002/jcc.20575>.
- [101] W. Tang, E. Sanville, G. Henkelman, A grid-based Bader analysis algorithm without lattice bias, *J. Phys. Condens. Matter.* 21 (2009) 084204. <https://doi.org/10.1088/0953-8984/21/8/084204>.
- [102] J. Tersoff, D.R. Hamann, Theory of the scanning tunneling microscope, *Phys. Rev. B.* 31 (1985) 805–813. <https://doi.org/10.1103/PhysRevB.31.805>.
- [103] D.E.P. Vanpoucke, G. Brocks, Formation of Pt-induced Ge atomic nanowires on Pt/Ge(001): a density functional theory study, *Phys. Rev. B.* 77 (2008) 241308. <https://doi.org/10.1103/PhysRevB.77.241308>.
- [104] M.J. Ungerer, D. Santos-Carballal, A. Cadi-Essadek, C.G.C.E. van Sittert, N.H. de Leeuw, Interaction of H₂O with the platinum Pt (001), (011), and (111) surfaces: a density functional theory study with long-range dispersion corrections, *J. Phys. Chem. C.* 123 (2019) 27465–27476. <https://doi.org/10.1021/acs.jpcc.9b06136>.
- [105] X. Wang, D. Santos-Carballal, N.H. de Leeuw, Density functional theory study of monoclinic FeNbO₄: bulk properties and water dissociation at the (010), (011), (110), and (111) surfaces, *J. Phys. Chem. C.* 125 (2021) 27566–27577. <https://doi.org/10.1021/acs.jpcc.1c05452>.
- [106] T. Jaumann, J. Balach, M. Klose, S. Oswald, J. Eckert, L. Giebeler, Role of 1,3-Dioxolane and LiNO₃ addition on the long term stability of nanostructured silicon/carbon anodes for rechargeable lithium batteries, *J. Electrochem. Soc.* 163 (2016) A557–A564. <https://doi.org/10.1149/2.1011603jes>.
- [107] J.S. Edge, S. O’Kane, R. Prosser, N.D. Kirkaldy, A.N. Patel, A. Hales, A. Ghosh, W. Ai, J. Chen, J. Yang, S. Li, M.-C. Pang, L. Bravo Diaz, A. Tomaszewska, M.W. Marzook, K.N. Radhakrishnan, H. Wang, Y. Patel, B. Wu, G.J. Offer, Lithium ion battery degradation: what you need to know, *Phys. Chem. Chem. Phys.* 23 (2021) 8200–8221. <https://doi.org/10.1039/D1CP00359C>.
- [108] Z. Lu, L. Yang, Y. Guo, Thermal behavior and decomposition kinetics of six

electrolyte salts by thermal analysis, *J. Power Sources*. 156 (2006) 555–559.
<https://doi.org/10.1016/j.jpowsour.2005.05.085>.

- [109] B. Ravdel, K. Abraham, R. Gitzendanner, J. DiCarlo, B. Lucht, C. Campion, Thermal stability of lithium-ion battery electrolytes, *J. Power Sources*. 119–121 (2003) 805–810. [https://doi.org/10.1016/S0378-7753\(03\)00257-X](https://doi.org/10.1016/S0378-7753(03)00257-X).